Lithium Insertion/Extraction into/from $LiMX_2O_7$ Compositions (M = Fe, V; X = P, As) Prepared via a Solution Method

Calin Wurm,[†] Mathieu Morcrette,[†] Gwenaelle Rousse,[‡] Loïc Dupont,[†] and Christian Masquelier*,[†]

Laboratoire de Réactivité et Chimie des Solides, CNRS UMR 6007, Université de Picardie Jules Verne, 33 rue Saint-Leu, 80039 Amiens Cedex, France, and Institut Laue Langevin, BP 156, F-38042 Grenoble Cedex 9, France

Received February 13, 2002. Revised Manuscript Received April 16, 2002

$LiFeP_2O_7$, $LiFeAs_2O_7$, and $LiVP_2O_7$ were prepared as pure microcrystalline powders via an aqueous solution route that allowed the formation of finely dispersed small particles. These three compounds, in which Fe or V is in the oxidation state +3, were evaluated as positive electrodes in lithium rechargeable batteries through galvanostatic, PITT, and GITT cycling modes and in situ X-ray diffraction. We show that the electrochemical activity of these materials is drastically enhanced by an intimate mixing of the pristine materials with conductive carbon, through ball-milling. This mandatory step resulted in producing amorphous Li−M−X−O domains at the surface of crystalline $LiMX_2O_7$ crystallites. A continuous voltage decrease is observed as lithium insertion proceeds into the amorphous part of the composite electrodes. Crystalline $LiMX_2O_7$ particles react with lithium through two-phase mechanisms, characterized by insertion plateaus located at 2.90 V for $LiFeP_2O_7$ (Fe^{3+}/Fe^{2+} couple), 1.99 V for $LiVP_2O_7$ (V^{3+}/V^{2+} couple), and 2.5 V for $LiFeAs_2O_7$. The Li-driven second phase is crystalline, with a larger unit cell in the case of isostructural $Li_{1+x}MP_2O_7$ (M = Fe, V). It is amorphous in the case of $Li_{1+x}FeAs_2O_7$, which shows, interestingly, a recrystallization process upon charging (when Li is extracted from $Li_2FeAs_2O_7$). Finally, lithium extraction from $LiVP_2O_7$ occurs at 4.26 V vs Li^+/Li (V^{3+}/V^{4+} couple) and leads through a two phase process to the new diphosphate VP_2O_7.

I. Introduction

Over the past decade, research on positive electrodes for lithium batteries mainly focused on the layered oxides $LiCoO_2$ and $LiNiO_2$, the spinel $LiMn_2O_4$, and all their substituting derivative compounds. Besides these "simple" oxides, polyanionic compounds built on PO_4 tetrahedra and MO_6 octahedra (M = transition metal) deserve special attention. Efforts toward this relatively novel class of intercalation hosts focused on iron-containing systems such as the Olivine $Li_{1-x}FePO_4$ [1−5] and NASICON compositions such as $Li_xFe_2(SO_4)_3$ [6] and $Li_3Fe_2(PO_4)_3$ [7−10] where reduction/oxidation of Fe^{3+}/Fe^{2+} occurs at potentials close to 3.45, 3.55, and 2.8 V vs Li/Li^+, respectively. These materials take full benefit from the inductive effect of $(XO_4)^{n-}$ tetrahedral groups that diminishes the covalence of the Fe−O bonds, hence increasing the operating voltage of the Fe^{3+}/Fe^{2+} redox couple vs Li compared to that in Fe_2O_3 for instance.[6] Moreover, several of these materials present attractive theoretical capacities: 128 mAh/g for A- and B-$Li_3Fe_2(PO_4)_3$,[8] 170 mAh/g for $LiFePO_4$.[1]

The $LiMX_2O_7$ compositions (M^{III} = Fe, V; X = P, As) of this study are less appealing in terms of theoretical capacity, because of their high X/M ratio that induces a strong weight penalty: 117 mAh/g for $LiVP_2O_7$, 113 mAh/g for $LiFeP_2O_7$, and 80 mAh/g for $LiFeAs_2O_7$ (to compare with 170 mAh/g for $LiFePO_4$). The redox couples that are accessible are Fe^{3+}/Fe^{2+} for $Li_{1+x}FeX_2O_7$ and, interestingly, V^{4+}/V^{3+} and V^{3+}/V^{2+} for $Li_{1\pm x}VP_2O_7$.[11] The aim of our work is to provide further understanding on how the relative positions of these redox couples

* To whom correspondence should be addressed. E-mail: Christian.Masquelier@sc.u-picardie.fr.
[†] Université de Picardie Jules Verne.
[‡] Institut Laue Langevin.

(1) Padhi, A. K.; Nanjundaswamy, K. S.; Goodenough, J. B. *J. Electrochem. Soc.* **1997**, *144* (4), 1188−1194.
(2) Ravet, N.; Goodenough, J. B.; Besner, S.; Simoneau, M.; Hovington, P.; Armand, M. 196th Electrochemical Society Meeting, Hawaï, 1999, Abstract No. 127. Ravet, N.; Besner, S.; Simoneau, M.; Vallée, A.; Armand, M. Can. Patent #2,270,771.
(3) Huang, H.; Yin, S. C.; Nazar, L. F. *Electrochem. Solid-State Lett.* **2001**, *4* (10), A170−A172.
(4) Yamada, A.; Chung, S. C.; Hinokuma, K. *J. Electrochem. Soc.* **2001,** *148* (3), A224−A229.
(5) Andersson, A. S.; Kalska, B.; Häggström, L.; Thomas, J. O. *Solid State Ionics* **2000**, *130*, 41−52.
(6) Manthiram, A.; Goodenough, J. B. *J. Solid State Chem.* **1987**, *71*, 349. Okada, S.; Nanjundaswamy, K. S.; Manthiram, A.; Goodenough, J. B. *Proceedings of the 36th Power Sources Conference*; Hyatt Cherry Hill: New Jersey, June 6−9, 1994.
(7) Padhi, A. K.; Nanjundaswamy, K. S.; Masquelier, C.; Okada, S.; Goodenough, J. B. *J. Electrochem. Soc.* **1997**, *144* (5), 1609−1613.
(8) Masquelier, C.; Padhi, A. K.; Nanjundaswamy, K. S.; Goodenough, J. B. *J. Solid State Chem.* **1998**, *135*, 228−234.
(9) Andersson, A. S.; Kalska, B.; Eyob, P.; Aernout, D.; Häggström, L.; Thomas, J. O. *Solid State Ionics* **2001**, *140*, 63−70.
(10) Morcrette, M.; Wurm, C.; Masquelier, C. *Solid State Sci.* **2002**, *4*, 239−246.
(11) Rousse, G.; Wurm, C.; Rodriguez Carvajal, J.; Morcrette, M.; Masquelier, C. *Int. J. Inorg. Mater.* **2001**, *3*, 881−887.

10.1021/cm020168e CCC: $22.00
Published on Web 05/18/2002

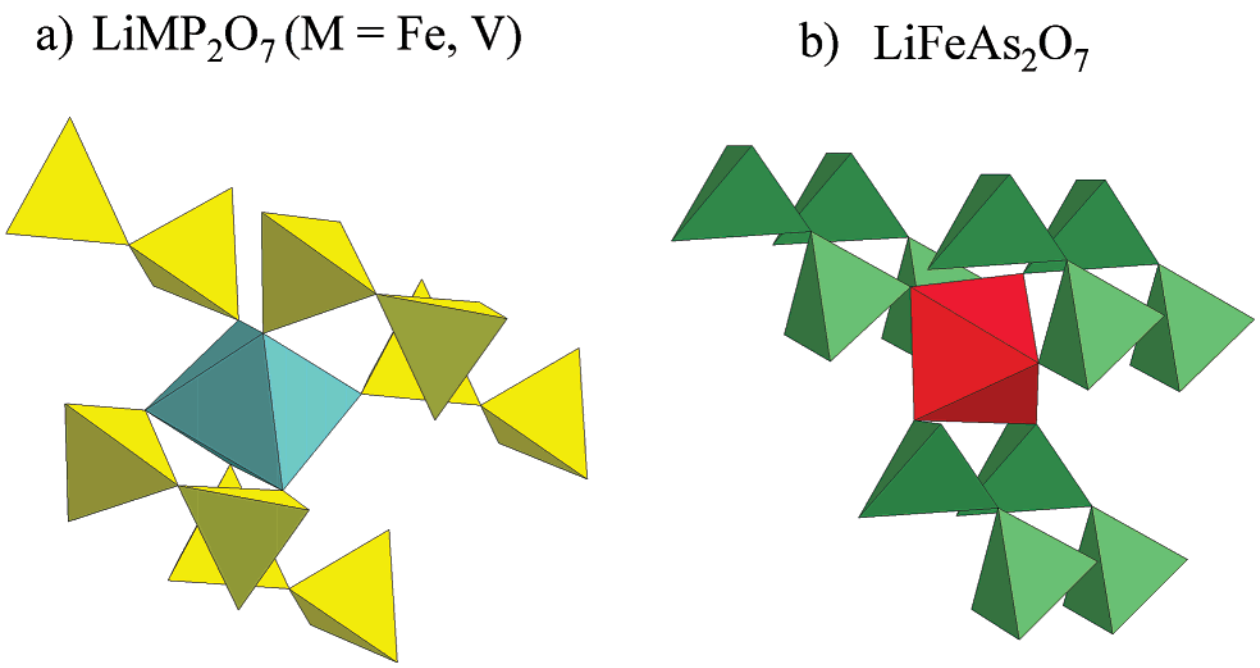

Figure 1. Crystallographic features of (a) $LiMP_2O_7$ (M = Fe, V) and (b) $LiFeAs_2O_7$.

would be influenced by the nature of the XO_4^{3-} anion and also by the crystal structure of the pristine materials. These compositions belong indeed to a wide family of $LiMX_2O_7$ 3-D frameworks[12,13] built on corner-sharing MO_6 octahedra and X_2O_7 groups delimiting an interstitial space, into which alkali cations may be inserted. $LiFeP_2O_7$ and $LiVP_2O_7$ are isostructural[14,15] and crystallize in the space group $P2_1$. The average Fe−O and V−O bond lengths are 2.00 Å, characteristic of iron or vanadium in the oxidation state +3 in an octahedral environment. As shown in Figure 1a, each FeO_6 (or VO_6) octahedron is linked to five different P_2O_7 groups, one of them acting as a "chelating" sequence around Fe (or V). These MP_2O_7 units are interconnected in a 3-D fashion so as to create cavities into which lithium ions are located in a distorted tetrahedral environment. $LiFeAs_2O_7$ adopts its own crystal structure,[16] described in the space group $C2$. There is in this case no bidentate corner sharing, and thus each FeO_6 octahedron is linked to six different As_2O_7 groups (Figure 1b). It should be noted that all these structure determinations were done from single crystal X-ray diffraction data and that only very little is known about their preparation as microcrystalline powders.

We describe in the first part of this paper the preparation of $LiFeP_2O_7$, $LiVP_2O_7$, and $LiFeAs_2O_7$ from a straightforward low-temperature route that allowed the obtainment of powders of small particle sizes. The second part deals with the electrochemical properties of the obtained powders. The study is focused on (i) investigating the possibility of lithium insertion into $LiVP_2O_7$ and $LiFeAs_2O_7$, (ii) optimizing the composite electrode preparations so as to operate on the maximum mass of the active material, (iii) determining the positions of the $M^{n+}/M^{(n-1)+}$ redox couples vs Li^+/Li and (iv) determining the mechanisms of lithium insertion through GITT, PITT, and in situ X-ray diffraction.

II. Experimental Section

$LiMX_2O_7$ powders were obtained from a general procedure that involved a mixing of soluble precursors in demineralized water (1 mol·L^{-1}) followed by a slow evaporation under continuous stirring to dryness before annealing the resulting solid at temperatures ranging from 300 to 800 °C. Specific conditions for each composition will be detailed in the next sections. These conditions were also monitored through the use of TG-DTA measurements performed with a Setaram TG-DTA 92 analyzer under air for $LiFeX_2O_7$ at 5 °C/min. In the case of $LiVP_2O_7$ (2 °C/min rate), the same type of analyzer was used, but in the TG configuration only to avoid the reaction of the Pt thermocouple with the 10% H_2/N_2 mix.

The morphology and size of the powders were controlled by scanning electron microscopy on a Philips XL30 FEG. SAED and TEM measurements were realized on a Philips CM12 STEM and on a Technai-20 for high resolution. Their specific surface was investigated through physisorption (adsorption) of N_2 at 77 K and BET calculations.[17] X-ray powder diffraction diagrams were obtained from overnight data collection either on a Philips PW 1729 diffractometer ($\theta-2\theta$) using Cu Kα radiation or on a Bruker D8 diffractometer ($\theta-\theta$) using Co Kα radiation.

Electrochemically driven structural changes were followed by means of an in situ electrochemical cell similar to that previously described,[20] the positive electrode material being directly deposited behind a beryllium window, which acted as the positive current collector. Once assembled, the cell was then mounted on a Scintag diffractometer operating in the

(12) Gabelica Robert, M.; Goreaud, M.; Labbe, P.; Raveau, B. *J. Solid State Chem.* **1982**, *45*, 389−395.
(13) Belkouch, J.; Monceaux, L.; Bordes, E.; Courtine, P. *Mater. Res. Bull.* **1995**, *30*, 149−160.
(14) Riou, D.; Nguyen, N.; Benloucif, R.; Raveau, B. *Mater. Res. Bull.* **1990**, *25*, 1363−1369.
(15) Lii, K. H.; Wang, Y. P.; Chen, Y. B.; Wang, S. L. *J. Solid State Chem.* **1990**, *86*, 143−148.
(16) Wang, S.; Wu, C.; Liu, S. *J. Solid State Chem.* **1994**, *113*, 37−40.
(17) Brunauer, P. H.; Emmett, P.; Teller, E. *J. Am. Chem. Soc.* **1938**, *60*, 309.
(18) Rodriguez-Carvajal, J. *Physica B* **1993**, *19*, 55. See http://www-llb.cea.fr/fullweb /powder.htm.
(19) Rietveld, H. M. *J. Appl. Crystallogr.* **1969**, *2*, 65.
(20) Patoux, S.; Dolle, M.; Rousse, G.; Masquelier, C. *J. Electrochem. Soc.*, accepted for publication, October 2001.

Bragg−Brentano geometry with Cu Kα radiation, and connected to the Mac-Pile system operating in GITT mode (after 1 h of cycling at the C/10 regime, a relaxing period was imposed for 1.5 h in order to record the X-ray diffraction pattern). A C/10 rate corresponds to a discharge within 10 h from $LiMX_2O_7$ to $Li_2MX_2O_7$ (1 Li inserted).

Electrochemical lithium insertion/extraction tests were performed in Swagelok type cells assembled in an argon-filled drybox with oxygen and water contents below 5 ppm. The negative electrode was a disk of lithium metal foil. A Whattman GF/D borosilicate glass fiber sheet, saturated with a 1 M $LiPF_6$ salt dissolved in 1:1 EC/DMC solution, was placed between the two electrodes. The composite positive electrodes contained 16.7 wt % acetylene black and 83.3% active material that were intimately mixed by ball-milling for various durations, between 15 and 240 min. For this ball-milling procedure (SPEC miller, 1400 rpm), 200 mg of active material and 40 mg of acetylene black were placed with a 4 g stainless steel ball in a stainless steel container of ∼40 mL. The typical mass of active material for each cell was between 10 and 20 mg. Lithium insertion/extraction was monitored with either a "Mac-Pile" or a "VMP" automatic cycling/data recording system (Biologic SA, Claix, France) operating in galvanostatic, GITT (galvanostatic intermittent titration technique), or PITT (potentiostatic intermittent titration technique) mode.

III. Materials Preparation

So far, most of the chemical routes described for the preparation of the $LiMX_2O_7$ (M = Fe, V; X = P, As) compositions of this study were aimed at preparing single crystals from either a hydrothermal route,[16] a solid-state reaction in a sealed silica tube,[15] or crystallization from a melt.[21] As we were interested in the electrochemical insertion/extraction of lithium into/from these structures, it was important to be able to fabricate these materials as pure microcrystalline powders, preferentially with small particle sizes, to compensate for their low intrinsic electronic conductivity and/or limit the macroscopic length of the Li diffusion paths.

Having these considerations in mind, we followed and developed in further detail a "wet" method proposed by Belkouch[13] based on mixing stoichiometric aqueous solutions of precursors followed by thermal treatments. This type of synthesis generally leads to pure compounds at a lower temperature than that required for solid-state reactions, generally resulting in the formation of smaller particles with higher surface area. The main advantage of the solution method we describe in this paper is the possibility of modifying the "solution parameters" such as concentration, pH, and so forth in order to monitor the solubility domains, avoid the precipitation of undesired species, or favor the precipitation of suitable intermediates. Optimized synthesis conditions should then improve the homogeneity of the precursors' mixing with an impact on the purity of the final product and on the lowering of the preparation temperature. These precursors have to be soluble (in water in our case), and the counterions have to be easy to decompose. The precursor ions chosen here are NH_4^+ and NO_3^-, decomposed into NH_3 and NO_x volatile species at ∼300 °C.

(IIIa) $LiFeP_2O_7$. The precursors used are LiH_2PO_4, $NH_4H_2PO_4$, and $Fe(NO_3)_3{\cdot}9H_2O$, each of them dissolved in demineralized water at concentrations of 1 mol·L^{-1}. TG-DTA experiments of the solid resulting from the evaporation of the solution at ∼100 °C are shown in Figure 2a. Different decomposition steps are observed between 100 and 400 °C, after which the crystallization of $LiFeP_2O_7$ occurs at ∼570 °C. This was confirmed by successive thermal treatments at temperatures ranging from 300 to 800 °C. At 300 °C for example, the obtained solid is amorphous. The choice of the pH of the starting solution (adjusted by NH_4OH or HNO_3) has an important impact on the nature of the solid formed at $T \sim$ 570 °C. As illustrated in Figure 3, acidic conditions lead to $LiFeP_2O_7$ systematically accompanied by slight amounts of impurities that we could not identify. A basic pH favors the precipitation of iron oxides or hydroxides, and under these conditions, a much higher temperature of annealing (∼750 °C) is necessary to obtain pure $LiFeP_2O_7$ (with large particle size). As shown in Figure 3, a slightly acidic, or close to neutral, pH of the initial aqueous mixture enables the formation of pure $LiFeP_2O_7$ at 570 °C with a specific surface area of 7.9 $m^2{\cdot}g^{-1}$. The lattice parameters refined in the space group $P2_1$ are listed in Table 1.

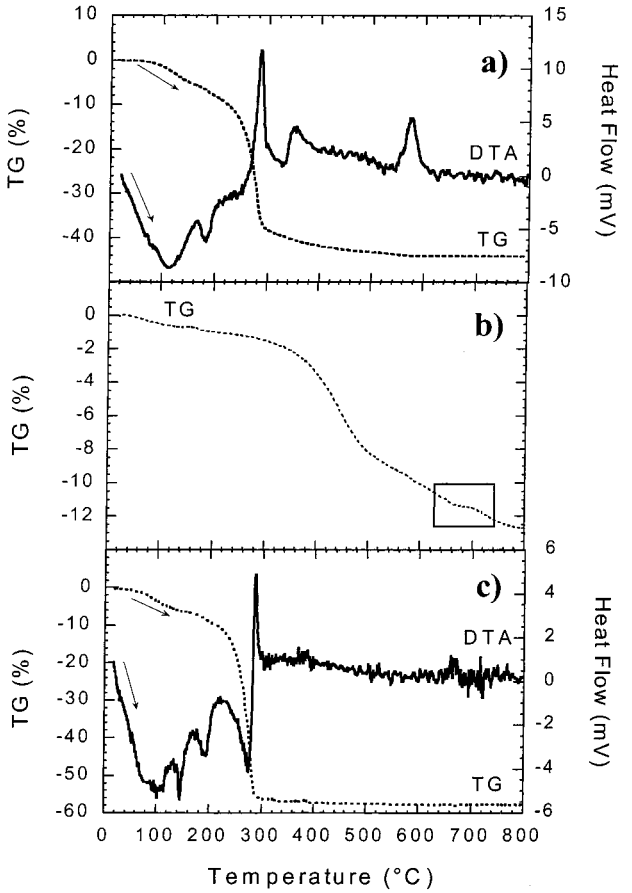

Figure 2. TG-DTA experiments of the solids issued from the evaporation at ∼100 °C of the precursor solutions used for the preparation of (a) $LiFeP_2O_7$ (5 °C/min), (b) $LiVP_2O_7$ (2 °C/min), and (c) $LiFeAs_2O_7$ (5 °C/min).

One of the advantages of this synthesis method is that, if needed, the obtained pure solid may be further annealed at higher temperature to adjust the size and specific area of the particles. As shown by the SEM photos of Figure 4, thin plates (∼2 μm) of $LiFeP_2O_7$ prepared at 570 °C lead to sintered (∼50 μm) particles at 800 °C with a much smaller surface area (<1 $m^2{\cdot}g^{-1}$). On the other hand, it turned out to be impossible to prepare pure $LiFeP_2O_7$ by classical solid-state reaction

(21) Genkina, A.; Maksimov, B. A.; Timofeeva, V. A.; Bykov, A. B.; Mel'nikov, O. K. *Sov. Phys. Dokl.* **1985**, *30* (10), 817−819.

Table 1. Preparation and Crystallographic Data for $LiMX_2O_7$ (M = Fe, V; X = P, As)

compd	temp (°C)	*a* (Å)	*b* (Å)	*c* (Å)	*β* (deg)	vol	space group
$LiFeP_2O_7$	570	4.821(1)	8.082(3)	6.936(2)	109.376(7)	254.9(1)	$P2_1$
$LiVP_2O_7$	650	4.812(1)	8.121(1)	6.945(1)	108.999(2)	256.6(1)	$P2_1$
$LiFeAs_2O_7$	300	6.677(2)	8.286(2)	4.741(1)	103.972(2)	254.5(1)	C_2

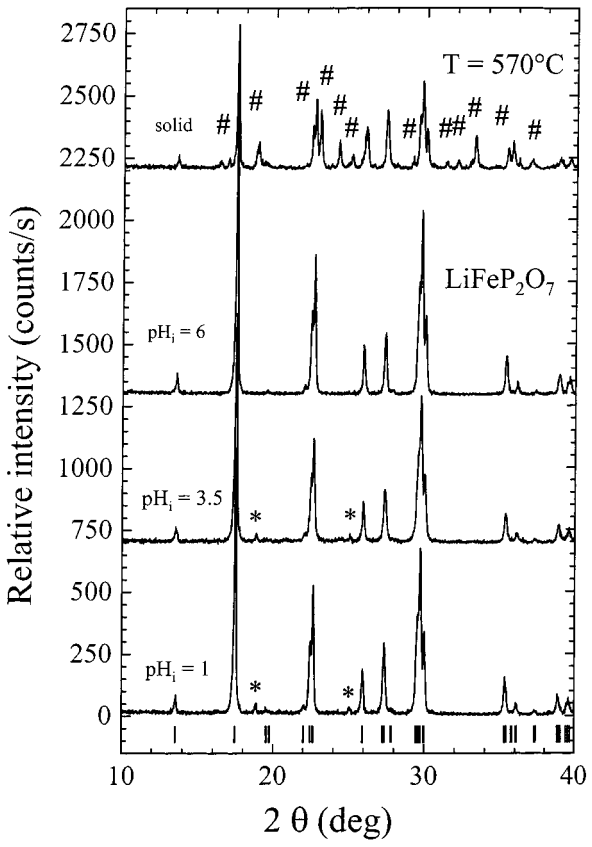

Figure 3. X-ray diffractograms (Cu Kα) on the influence of the pH of the starting solution on the purity of the obtained $LiFeP_2O_7$ powder. The solid-state preparation at 570 °C is also represented for comparison. The symbol (∗) refers to impurities that we could not index. Most of the symbols (#) refer to Fe_2O_3 and $LiPO_3$ impurities.

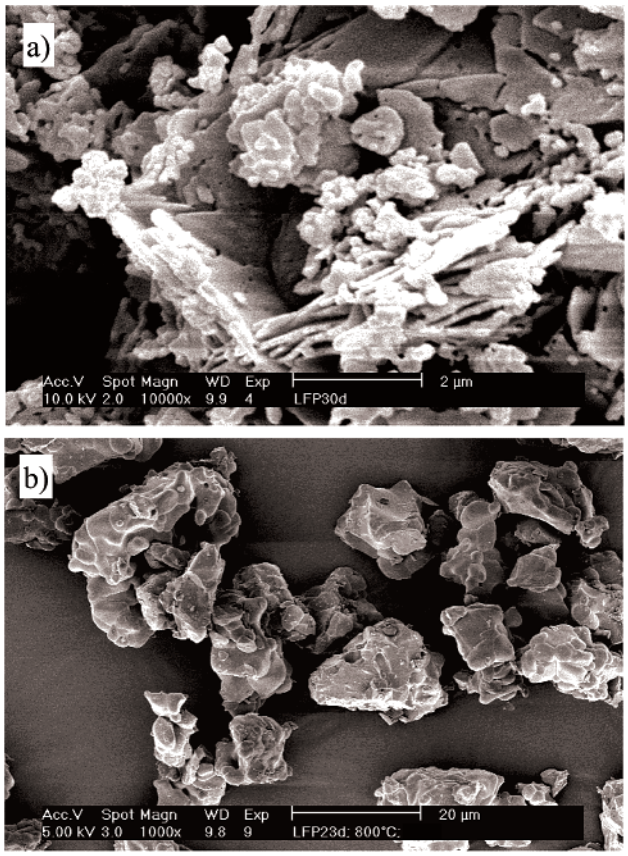

Figure 4. SEM images of $LiFeP_2O_7$ prepared at low (a: 570 °C) and high temperature (b: 800 °C)

at temperatures lower than 750 °C. It is always accompanied by impurities such as $Fe(PO_3)_3$, Fe_2O_3, $LiPO_3$, and so forth (Figure 3).

(IIIb) $LiVP_2O_7$. The precursors used were LiH_2PO_4, $NH_4H_2PO_4$, and NH_4VO_3. This latter was used at the concentration 0.2 mol·L^{-1}, as it is only slightly soluble in water. The use of V^{5+}-containing precursors implies that the annealing of the resulting precipitate, once the solvent evaporated, should be done under reduced atmosphere to yield V^{3+}-containing $LiVP_2O_7$. As shown by the TG plot of Figure 2b (no DTA, see Experimental Section) recorded at 2 °C/min under a N_2/H_2 flow (10% H_2), there is a continuous weight loss (volatile species + reduction of vanadium ions) as the temperature increases with, interestingly, a slight step at 650−675 °C. This experiment paved the way for carefully optimizing the firing temperature, that is, as further demonstrated by the X-ray diffraction patterns of Figure 5, restricted to a limited range between 650 and 675 °C. Below or above this temperature range, impurity peaks (different in each case) are detected, with V^{4+}-containing compounds below 650 °C and V^{2+}-containing materials above 675 °C. The $LiVP_2O_7$ solid obtained at 650 °C has a rather small specific area of 2.6 $m^2 \cdot g^{-1}$ and is isostructural with $LiFeP_2O_7$ with the lattice parameters, refined in the space group $P2_1$, listed in Table 1.

(IIIc) $LiFeAs_2O_7$. The precursors used are Li-(CH_3COO), $NH_4H_2AsO_4$, and $Fe(NO_3)_3 \cdot 9H_2O$, dissolved in demineralized water. As suggested by the TG-DTA plots of Figure 2c, and further confirmed by annealing the solid issued from the evaporation, pure $LiFeAs_2O_7$ is already formed at 300 °C in the shape of very small needles (∼200 nm long, diameter 50 nm) with the specific surface area 32 $m^2 \cdot g^{-1}$. An acidic pH (∼5) of the starting solution was needed to avoid the precipitation of a solid of different composition that prevented the formation of pure $LiFeAs_2O_7$. As shown in Figure 6, further annealing of the solid obtained at 300 °C results in a better crystallinity as well as in a significant decreasing of its specific surface area: 2.4 $m^2 \cdot g^{-1}$ (Table 2). At temperatures higher than 700 °C, decomposition starts to occur. Note that we never succeeded in preparing pure $LiFeAs_2O_7$ via an initial mixture of solid precursors.

IV. Electrochemistry

As described in the introductory part of this paper, $LiMX_2O_7$ compositions (M = Fe, V; X = P, As) are built

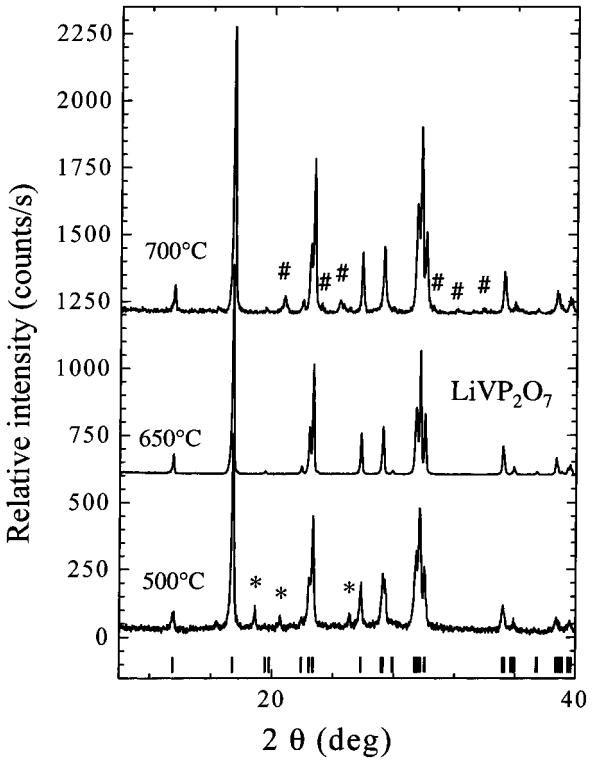

Figure 5. X-ray diffraction patterns (Cu Kα) of $LiVP_2O_7$ powders obtained at 500, 650, and 700 °C.

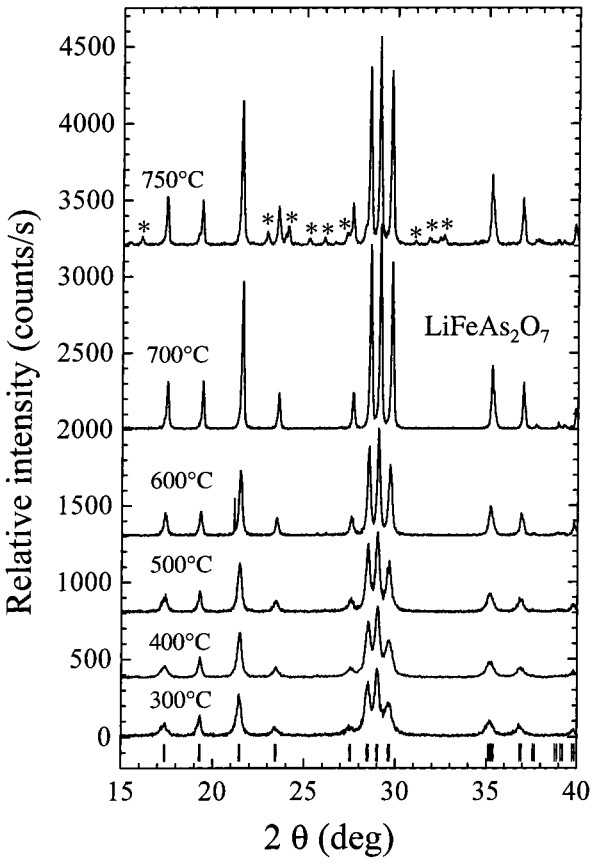

Figure 6. X-ray diffraction patterns (Cu Kα) of $LiFeAs_2O_7$ powders obtained at different temperatures.

from a 3-D framework of MO_6 octahedra and X_2O_7 groups delimiting a large interstitial space that can accommodate additional alkali cations. So far, the only reported studies related to possible electrochemical insertion or extraction from/into these structures are those of Padhi et al. on $Li_{1+x}FeP_2O_7$ (Fe^{3+}/Fe^{2+})[7] and ours on $Li_{1-x}VP_2O_7$ (V^{4+}/V^{3+}).[11] In this paper, their electrochemical properties toward lithium insertion or extraction were investigated by means of various cycling modes (galvanostatic, GITT, PITT), coupled with structural investigations performed through in situ or ex situ X-ray diffraction.

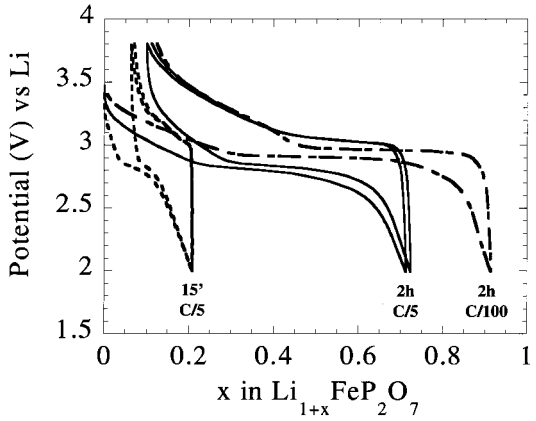

Figure 7. Influence of regime and ball-milling of carbon/active material mixtures on the electrochemical properties of $LiFeP_2O_7$.

Table 2. Specific Area Determined by the BET Technique for $LiFeAs_2O_7$ Prepared at Different Temperatures

temp (°C)	S (m^2/g)
300	32.3
400	28.9
500	17.5
600	8.2
700	2.4

(IVa) Insertion of Lithium into $LiFeP_2O_7$: $Li_{1+x}FeP_2O_7$. Padhi was the first to show the reversible insertion of 0.5 lithium into $LiFeP_2O_7$ at an average potential of 2.9 V vs Li for the Fe^{3+}/Fe^{2+} redox couple. This was done on a sample of high crystallinity prepared from solid-state reaction at 850 °C. We reinvestigated in detail the electrochemical properties of $LiFeP_2O_7$ as a positive electrode in lithium cells. The material of this study was prepared at a much lower temperature, that led to particles of higher specific surface area (~8 $m^2 \cdot g^{-1}$) than those obtained by high-temperature solid-state reaction. At first sight, standard electrode preparation coupled with a fast discharge regime of C/5 lead to disappointing behavior, as only 0.2 lithium could be inserted with a large polarization (Figure 7). As briefly mentioned by Padhi[7] and recently further developed for $Li_{3+x}Fe_2(PO_4)_3$,[10] intimate mixing between conductive carbon and iron phosphates (mostly insulating) is of peculiar importance to optimize their electrochemical activity. This was nicely demonstrated by Ravet[2] and Huang,[3] who reported excellent reversibility, close to full theoretical capacity, for $LiFePO_4$ particles embedded into a conductive carbon matrix that had been chemically deposited. As shown in Figure 7, mechanical milling of the composite electrode mixture $LiFeP_2O_7$/acetylene black (16.7 wt % carbon) is very effective for this class of compounds, where close to theoretical capacity (90% on first discharge) is reached at a low regime of C/100. For this powder, 2 h of ball-milling was set as the optimum time. Note that we never succeeded in reaching more than 65% of the theoretical capacity

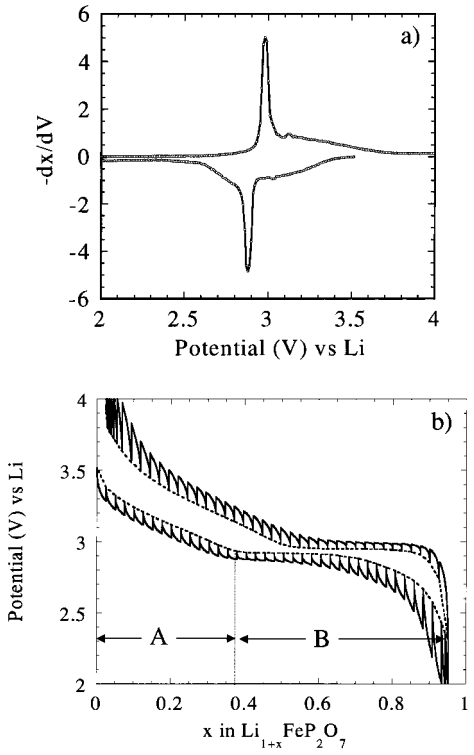

Figure 8. Potentiodynamic (a) and galvanostatic intermittent titration (b) curves of $LiFeP_2O_7$.

by ball-milling $LiFeP_2O_7$ particles obtained from solid-state reaction at 800 °C.

Slow potentiodynamic (PITT, Figure 8a) and GITT (Figure 8b) experiments reveal the existence of two distinct regions, noted A and B, as x increases in $Li_{1+x}FeP_2O_7$. In the A region ($0 \leq x \leq 0.4$), a slight continuous decrease in the cell voltage (between 3.5 and 2.9 V) is observed as x increases. In the B region ($0.4 \leq x \leq 0.8$), one observes a "shy" intercalation plateau located at 2.92 V vs Li^+/Li. Thus, in light of these results, a single-phase redox process was expected at the beginning of lithium intercalation followed by a two-phase region until the end of discharge.

We went deeper in the understanding of this electrochemical behavior by performing an in situ X-ray diffraction study for a full discharge/charge cycle. The obtained diffraction patterns are plotted in Figure 9. In the first part of the discharge process (A region), there is no shift in the positions of the diffraction peaks, which at first sight may be interpreted as a solid solution process with extremely small variations in the lattice parameters. Although this hypothesis may not be totally excluded, the A region is more likely a signature of lithium electrochemical reaction with an amorphous $Fe^{III}-P-O$ solid formed during the ball-milling of the composite electrode. Indeed, as we recently showed,[22] this kind of amorphous composition does react (reversibly) with lithium at average potential values of 3 V. This interpretation will be further exemplified in the next section for the redox behavior of $LiFeAs_2O_7$. Upon further discharge ($x \geq 0.4$, B region"), there is no doubt that the process at 2.92 V vs Li^+/Li is a two-phase reaction. One observes the appearance of new diffraction

(22) Masquelier, C.; Reale, P.; Wurm, C.; Morcrette, M.; Dupont, L.; Larcher, D. *J. Electrochem. Soc.*, submitted.

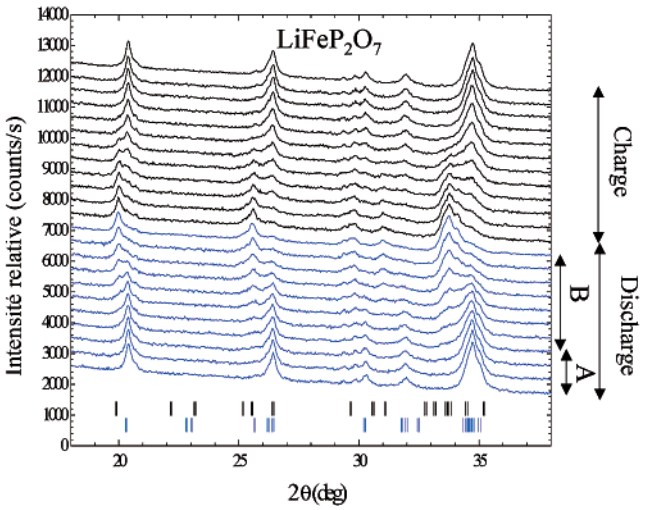

Figure 9. In situ X-ray diffraction (Co Kα) study for a full discharge/charge cycle on an $LiFeP_2O_7$ electrode at C/10. Vertical bars correspond to the Bragg positions of $LiFeP_2O_7$ (upper) and $Li_2FeP_2O_7$ (lower).

peaks at lower diffraction angles, coupled with the disappearance of those of the pristine phase. This new Li-intercalated $Li_{1+x}FeP_2O_7$ phase was indexed in the same space group as that of $LiFeP_2O_7$, with a 5% bigger unit-cell volume. The two above processes are highly reversible, as suggested by the electrochemical data of Figure 8a and further confirmed by the in situ XRD pattern of the solid obtained after reoxidation to $LiFeP_2O_7$ (Figure 9).

(IVb) Insertion of Lithium into $LiFeAs_2O_7$: $Li_{1+x}FeAs_2O_7$. As shown by the galvanostatic data of Figure 10a (5 cycles at a regime of C/20), $LiFeAs_2O_7$ is also active toward lithium insertion in the 3.5−2 V voltage window. The first discharge looks similar to that of $LiFeP_2O_7$, with two main regions clearly distinguishable: a continuous decrease in the potential occurs first (A region) prior to an intercalation plateau (B region), located this time at 2.45 V vs Li^+/Li. After the first reduction, the situation is far more complex, though, as (i) a large overvoltage occurs on the first charge for which the redox plateau is less featured, (ii) the second discharge has a different shape (more continuous) at a higher average potential than that for the first one, and (iii) the plateau has mostly disappeared after the fifth cycle, for which the overvoltage between discharge and charge is small. A tentative explanation of this complex series of phenomena is developed below.

The information contained in Figure 10b is very instructive, as it compiles the electrochemical behavior of two different pristine $LiFeAs_2O_7$ samples, prepared at 300 °C (dotted lines) and 600 °C (full lines), each of them ball-milled with 16.7% carbon SP for 60 or 240 min. It is obvious that the number of exchanged electrons between the A and B regions on first discharge closely depends on the composite electrode itself: the lower temperature of preparation of pristine $LiFeAs_2O_7$ and, to a lesser extent, the longer duration of ball-milling with carbon lead to a significant increase in the A region domain at the expense of the B one. The proportions of these two domains as a function of ball-milling time are indicated in the inset of Figure 10b.

Our interpretation of the existence of the A region is that the ball-milling of the $LiFeAs_2O_7$/carbon mixtures

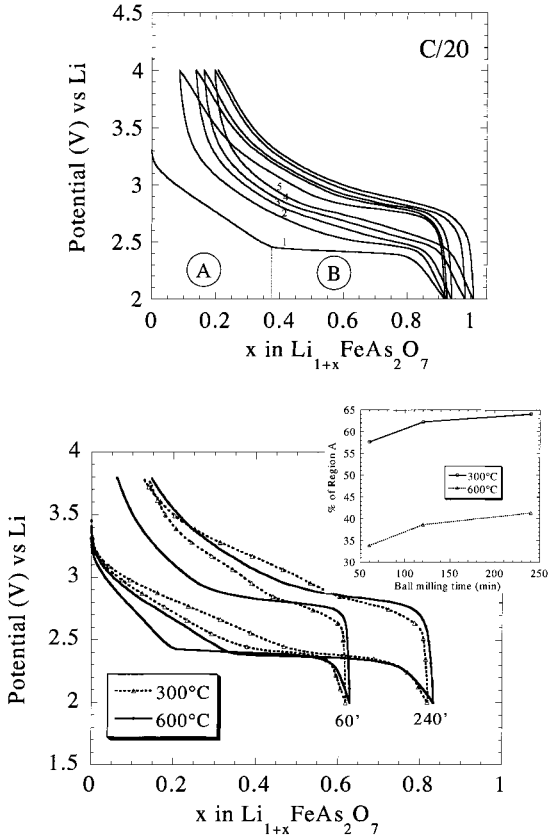

Figure 10. Electrochemical behavior of $LiFeAs_2O_7$: (a) the first five galvanostatic cycles of at C/20; (b) as a function of sintering temperature preparation (300 and 600 °C) and ball-milling time (1 and 4 h). In the inset, the percentage of region A calculated is represented as a function of ball-milling time for both temperatures.

induces a partial amorphization and that the obtained composite electrode contains an amorphous Li−Fe−As−O solid and small particles of crystalline $LiFeAs_2O_7$. This is supported by the TEM study realized on the $LiFeAs_2O_7$/C sample ball-milled for 2 h. In the HRTEM image of Figure 11, two different regions noted A and B, which are amorphous and crystallized, respectively, are clearly visible. The EDS spectrum realized on each region shows that they both contain iron and arsenic. Moreover, according to the EELS spectrum, the amorphous region A contains carbon while this element is missing for the crystallized region B. By gathering EELS, EFTEM, and EDS mapping, carbon and iron maps were realized. The mapping evidences the carbon nodules observed on the C map but missing on the Fe map. On the contrary, the crystalline region B is visible on iron mapping and absent from the carbon one. Finally, the amorphous A region is observed on both maps. According to these experiments, the ball-milling of the LFA induced the creation of an amorphous Li−Fe−As−C composite phase 50−100 Å thick (region A) surrounding remaining crystallized $LiFeAs_2O_7$ grains of less than 50 Å (region B).

This series of observations is also supported by the in situ X-ray diffraction data plotted in Figure 12. The diffractograms recorded during lithium insertion in the A region are all the same, with neither changes in intensities nor shifts in diffraction peak positions. This was carefully checked by integration of the three diffraction peaks in the $28.5 < 2\theta < 32$ region. The redox

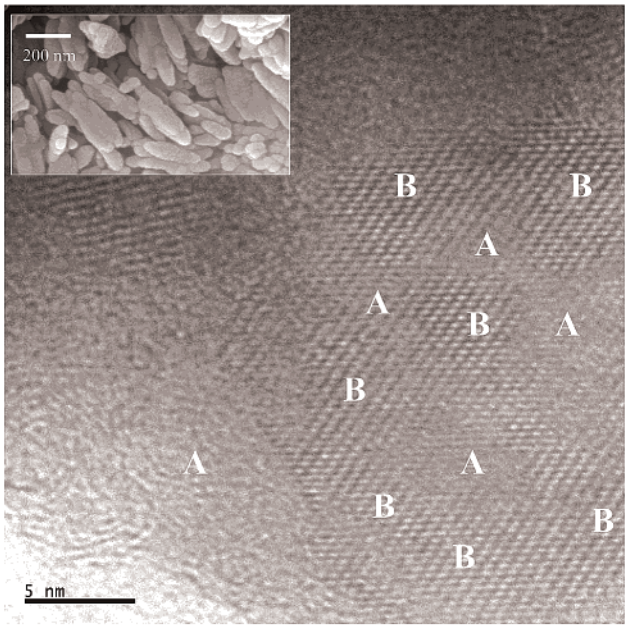

Figure 11. HRTEM image of the $LiFeAs_2O_7$/C composite electrode prior to electrochemical cycling. The A and B marks delimit amorphous and crystalline domains, respectively. In the inset, an SEM image of the pristine needle-like $LiFeAs_2O_7$ crystallite is shown.

process encountered in the A region, that is, insertion of lithium into an amorphous matrix, is similar to that mentioned in the previous section for $LiFeP_2O_7$ and to those identified on the numerous ball-milled iron phosphates we recently investigated: $Li_3Fe_2(PO_4)_3$ [10] and, more interestingly, amorphous $FePO_4 \cdot 2H_2O$.[22]

In the B region of the first discharge, one observes an intercalation plateau (two-phase process) located at 2.5 V vs Li^+/Li, as clearly shown by the GITT experiment (Figure 13). Once again, ex situ electron diffraction and in situ X-ray diffraction gave us the clue for a reasonable explanation of what occurs within this two-phase domain. The first obvious observation is that, within the B region, the intensities of $LiFeAs_2O_7$ diffraction peaks progressively vanish without any peak position shift. As an illustration, Figure 12 also shows the variation of the relative intensity of the diffraction peaks located at 29° vs the number x of "inserted" lithium atoms. This is somewhat "classical" for a two-phase reaction, but the peculiar behavior of this system is that the second phase is not crystalline, as no new diffraction peaks appear within the whole discharge. Indeed, SAED shows that the solid obtained at the end of discharge down to $x \sim 0.95$ (Figure 13) is fully amorphous. Note that, for the in situ XRD experiment performed on a sample that had been only moderately ball-milled, the remaining XRD peaks are due to the fact that the reaction was not complete ($x \sim 0.75$). This is supported by the nice extrapolation of the disappearance of the (001) peak toward $x = 1$ in Figure 12.

More intriguing even is what we observed during recharge of the mostly amorphous solid obtained after the biphasic process at 2.5 V. The in situ X-ray diffraction data plotted in Figure 12 show a very nice recrystallization of the parent $LiFeAs_2O_7$ compound, further confirmed by ex situ electron diffraction. It is interesting to note that this process is located at ~300 mV higher

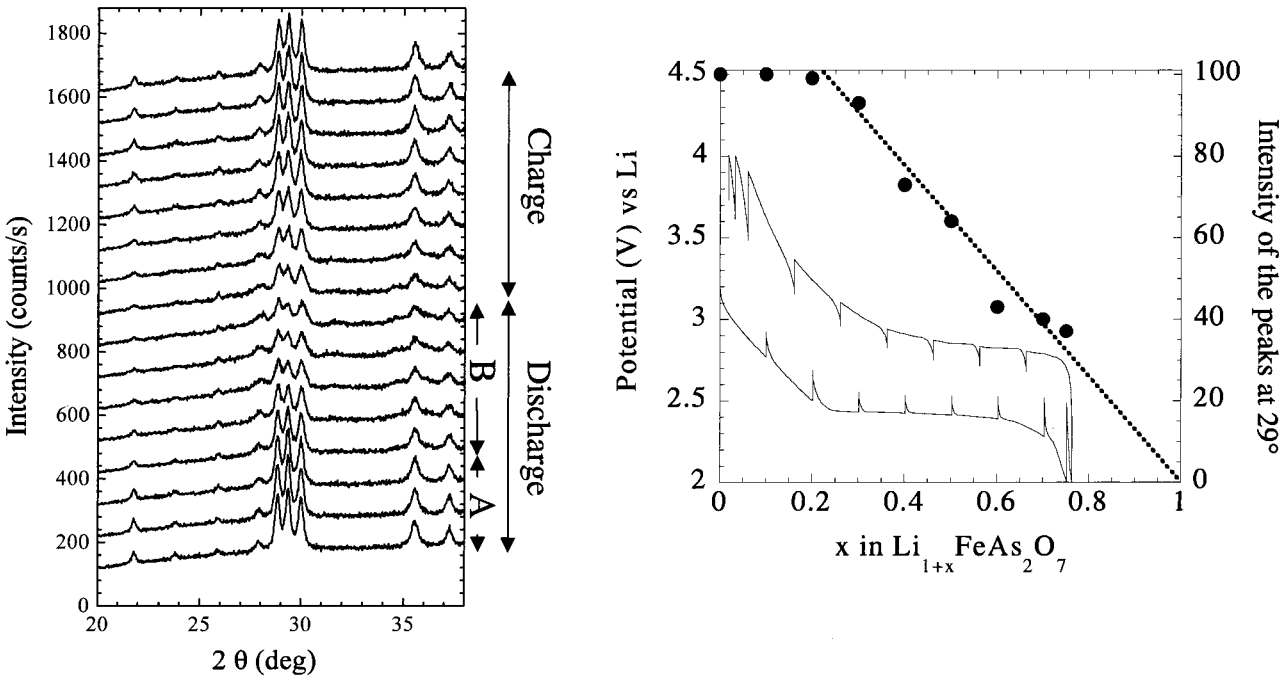

Figure 12. In situ X-ray diffraction study (Cu Kα) for a full discharge/charge cycle on a $LiFeAs_2O_7$ electrode at C/10.

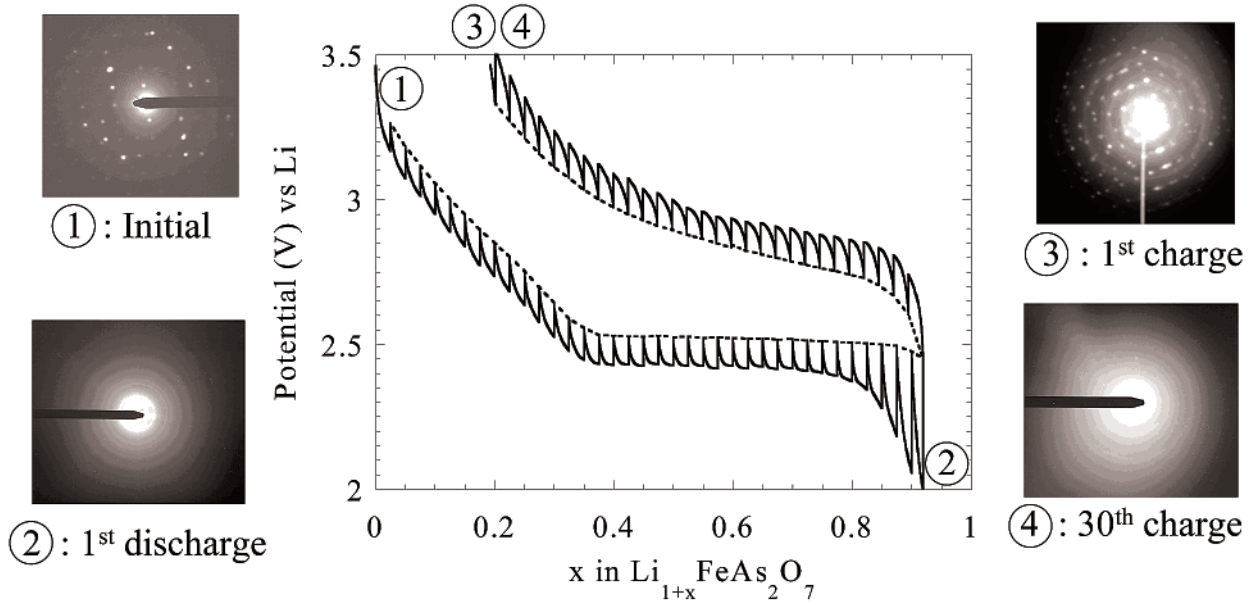

Figure 13. TEM images of the pristine $LiFeAs_2O_7$ electrode, after one discharge, after one charge, and after 30 cycles.

than the amorphization during discharge. This 300 mV overvoltage is much more pronounced than that classically needed to initiate germination of a new phase in a two-phase process (~100 mV overvoltage in the first galvanostatic curves of $Li_4Ti_5O_{12}$ and $LiCoO_2$). A parallel might be drawn between what we observe for $LiFeAs_2O_7$ and the behavior of stoichiometric and highly crystalline $LiMn_2O_4$ that presents 3.3 V (on discharge) and 3.95 V (on charge) anomalies associated with a spinel to double-hexagonal phase transformation.[23] The 650 mV polarization is due to the low kinetics of the phase transformation that induces a complete transformation of the network in terms of the MnO_6 arrangement.

(23) Palacin, R.; Rousse, G.; Morcrette, M.; Dupont, L.; Masquelier, C.; Chabre, Y.; Hervieu, M.; Tarascon, J. M. *J. Power Sources* **2001**, *97*−*98*, 398−401.

Figures 10a and 14 summarize the electrochemical behavior of the "$LiFeAs_2O_7$" electrode upon cycling. As already mentioned, one immediately notes a progressive disappearance of the 2.5 V discharge plateau on cycling: it continuously shifts toward higher potential values (up to 2.65 V) and continuously vanishes to the benefit of a new incremental capacity peak located at 2.8 V. From TEM observation on the electrode obtained after 30 cycles, and by analogy with what we recently found for the electrochemical behaviors of amorphous $Li_xFeXO_4 \cdot H_2O$ (X = P, As),[22] we determined that the overall electrode is less and less crystalline after each charge, because of the repeated crystallization/amorphization processes upon cycling. Once there is not enough crystalline $Li_xFeAs_2O_7$ "germ" particles left at the end of discharge, there is no recrystallization occurring on

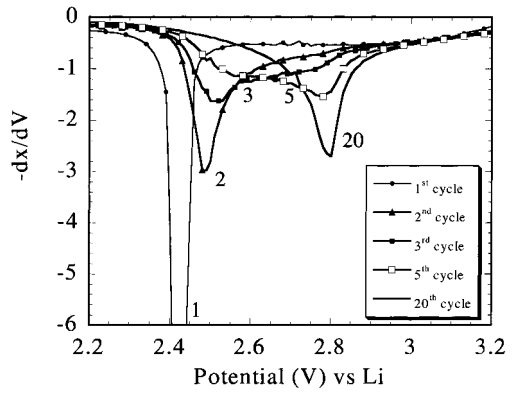

Figure 14. Incremental capacity versus voltage curves for the first, second, third, fifth, and twentieth cycles of $LiFeAs_2O_7$.

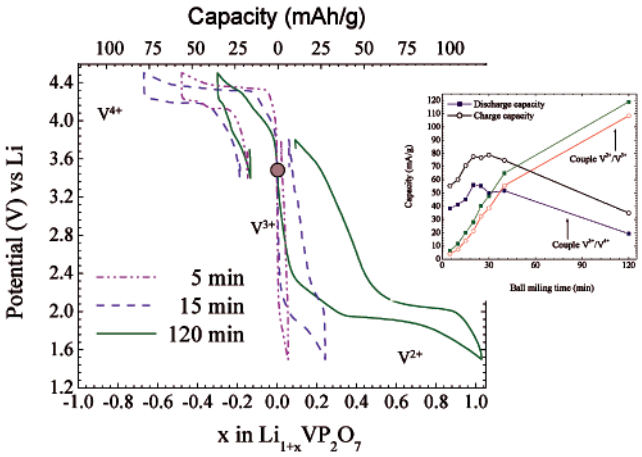

Figure 15. Galvanostatic cycling of $LiVP_2O_7$ at high and low potential. In the inset of the figure, the capacities as a function of ball-milling time are reprensented for both processes.

subsequent charges. Interestingly, the amorphization does not induce significant irreversible capacity and the electrode is remarkably stable on cycling, as for $Li_xFePO_4 \cdot 2H_2O$.[22] The average potential observed for the amorphous Li−Fe−As−O electrode (~2.90 V) translates the inductive effect of As onto the Fe^{3+}/Fe^{2+} redox couple. The strength of this inductive effect is very similar to that observed in iron phosphates because of the fact that As and P have similar electronegativities.[8]

(IVc) Insertion or Extraction of Lithium in/from $LiVP_2O_7$: $Li_{1\pm x}VP_2O_7$. The peculiar behavior of $LiVP_2O_7$ is illustrated by the fact that V^{3+} can be either reduced to V^{2+} by lithium insertion or oxidized to V^{4+} by lithium extraction (Figure 15). The mechanisms of these two redox processes were investigated through slow potentiodynamic and GITT experiments. As for $LiFeP_2O_7$ (to which $LiVP_2O_7$ is isostructural) and $LiFeAs_2O_7$, ball-milling of the pristine material with carbon was necessary in order to favor electronic contact in the positive electrode. The X-ray diffraction patterns of the obtained composite electrodes show no phase transformation besides a slight enlargement of most diffraction peaks.

When $LiVP_2O_7$ is first reduced (V^{3+} to V^{2+}), the galvanostatic data (regime of C/20) plotted in Figure 15 show that the theoretical capacity of one inserted lithium per vanadium is reached for a $LiVP_2O_7$/carbon mixture that had been ball-milled for 2 h. On the other hand, standard electrode preparation leads to no electrochemical activity. For the optimized composite electrode, the general shape of the voltage profile is similar to that of $LiFeP_2O_7$ but at significantly different potential values. There is first a continuous decrease in the voltage down to 2.0 V between $x = 0$ and $x = 0.3$ in $Li_{1+x}VP_2O_7$ (the A region). Second, an intercalation plateau ranging from $x = 0.3$ to $x \sim 0.9$ is observed, whose equilibrium potential, 1.99 V vs Li^+/Li, was determined through careful GITT and slow potentiodynamic (Figure 16a) experiments. The signatures of this equilibrium potential are (i) a constant intercalation/deintercalation potential in the GITT curve and (ii) a sharp peak of incremental capacity. Both methods give the same value for the V^{3+}/V^{2+} redox couple, equal to 1.99 V, but it is worth noting that the GITT experiment lasted for 2 months whereas the potentiodynamic discharge was performed within 24 h!

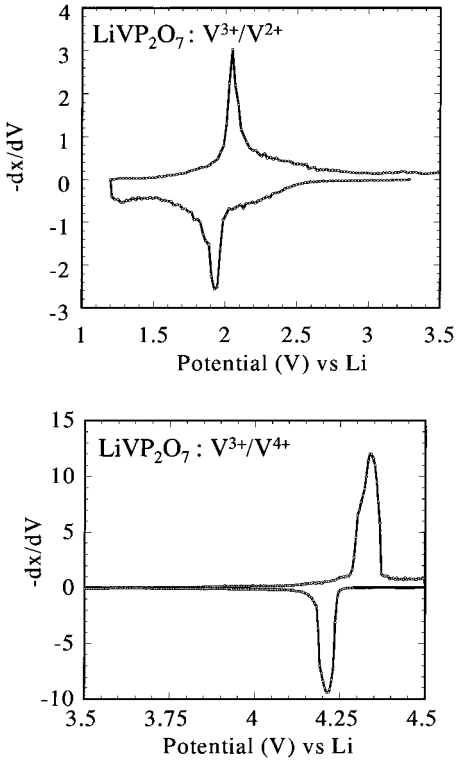

Figure 16. PITT data for (a) the insertion of lithium into $LiVP_2O_7$ (V^{3+}/V^{2+}) and (b) the extraction of lithium from $LiVP_2O_7$ (V^{4+}/V^{3+}).

In situ X-ray diffraction during a full discharge cycle is shown in Figure 17. In the first part of the discharge process (A region), there is, as for $Li_{1+x}FeP_2O_7$, no shift in the peak positions of the pristine $LiVP_2O_7$ that suggests a first process of "insertion" in the amorphous matrix produced by the ball-milling with carbon. As soon as the intercalation plateau at 2.0 V vs Li^+/Li is reached ($x \geq 0.3$, B region) and despite the somewhat poor quality of the obtained XRD patterns, there is no doubt that the XRD peaks of $LiVP_2O_7$ progressively vanish for the benefit of those of a new lithiated $Li_{1+x}VP_2O_7$ phase with a bigger unit cell. The two above processes are reversible, as suggested by the electrochemical data of Figure 15 and further confirmed by the in situ XRD pattern of the solid obtained after reoxidation to $LiVP_2O_7$.

When $LiVP_2O_7$ is first charged (oxidation of V^{3+} to V^{4+}), the galvanostatic data (recorded at a regime of C/20) plotted in Figure 15 show that lithium may be extracted at an interesting potential of 4.26 V vs Li^+/Li

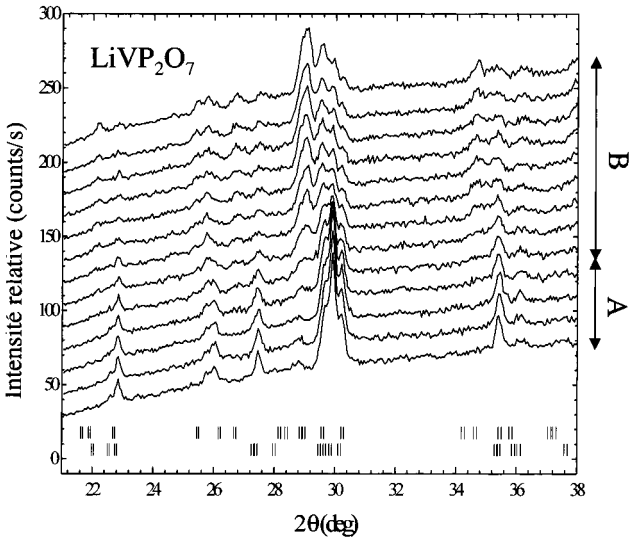

Figure 17. In situ X-ray diffraction study for a full discharge/charge cycle on a $LiVP_2O_7$ electrode at C/40 (V^{3+}/V^{2+}).

(Figure 16b). One immediately notes that, although ball-milling with conductive carbon is required to get electrochemical activity out of this material, there is an optimum duration of ball-milling (~20 min) after which the electrochemical properties are significantly altered. Indeed the ball-milling favors electrical contact between conductive carbon and electrochemically active $LiVP_2O_7$ particles but also reduces the size of these particles, hence creating surface defects that favor electrolyte decomposition and/or V^{4+} dissolution. From chemical analysis, we found significant amounts of V^{4+} dissolved in the electrolyte at the end of charge. The well-defined potential plateau at 4.26 V is characteristic of a two-phase process, between $LiVP_2O_7$ and VP_2O_7. We recently showed[11] from ex situ synchrotron X-ray diffraction that the end-member VP_2O_7 prepared either electrochemically or chemically (oxidation of $LiVP_2O_7$ from NO_2BF_6) adopts a crystal structure very similar to that of $LiVP_2O_7$. The parent $[VP_2O_7]$ framework is maintained during lithium extraction, but significantly distorted, which can be at the origin of the important polarization of the cell between galvanostatic charge and discharge.

V. Conclusion—Inductive Effect

Having demonstrated the possible intercalation of up to one lithium (reduction $M^{3+} \rightarrow M^{2+}$) with the three structures $LiFeP_2O_7$, $LiFeAs_2O_7$, and $LiVP_2O_7$, it was tempting to summarize the obtained data so as to compare the values of the redox potentials at which electrochemical reduction occurs (Figure 18). Each of the three materials displays two distinct regions, which we labeled A and B.

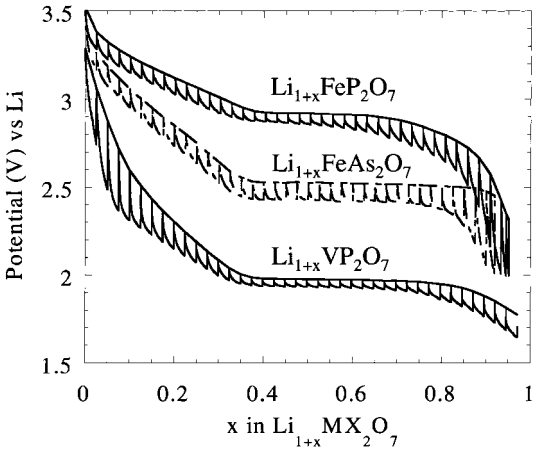

Figure 18. Comparison of the first reduction curves in GITT discharges of $LiFeP_2O_7$, $LiFeAs_2O_7$, and $LiVP_2O_7$.

The A region corresponds to lithium uptake in an amorphous layer at the surface of the grain generated by the ball-milling of the pristine material with conductive carbon. Interestingly, the average voltage of such a process is located at ~3.2 V vs Li for amorphous "$LiFeP_2O_7$". This may be nested in the fact that the P/Fe ratio is high and thus generates a strong inductive effect on the local Fe−O bonds. Similarly, we recently observed[22] that the average voltage of Li uptake into amorphous $Fe_4(P_2O_7)_3 \cdot nH_2O$ (~3.2 V) is higher than that for uptake into amorphous $FePO_4 \cdot nH_2O$ (~3.0 V). The larger continuous voltage decrease in the A region for $LiFeAs_2O_7$ in the first discharge comes from the large hysteresis within the B region where amorphization/recrystallization of $Li_{1+x}FeAs_2O_7$ occurs. On cycling, the average voltage of this cell shifts toward higher values, close to 2.85 V. As mentioned in a previous paper,[8] the overall inductive effects of P and As on the position of the Fe^{3+}/Fe^{2+} redox couple are more or less identical, because of their similar electronegativities.

The B region corresponds to two-phase reactions that provide interesting values to compare for the Fe^{3+}/Fe^{2+} and V^{3+}/V^{2+} redox couples. Isostructural $LiFeP_2O_7$ and $LiVP_2O_7$ behave in a very similar way, with a new lithiated $Li_{1+x}MP_2O_7$ form growing at the expense of the pristine $LiMP_2O_7$, at 2.99 and 2.00 V for M = Fe and V, respectively. This ~1.0 V difference between Fe^{3+}/Fe^{2+} and V^{3+}/V^{2+} redox couples is similar to that observed between $Li_{3+x}Fe_2(PO_4)_3$ [8] (2.8 V) and $Li_{3+x}V_2(PO_4)_3$ (1.9 V).

Acknowledgment. We thank the FEI company for access to their TEM facilities. Pr. J.-M. Tarascon and Dr. Y. Chabre are gratefully acknowledged for their critical and constructive reading of the manuscript.

CM020168E